

S1 Fractions of samples above detection limits

The following Figures S1–S3 illustrate the fraction of the measurements (for monthly bins), for which the chromatographic peaks were identified and quantified by the software integration settings (detectable peaks). They illustrate the increasing presence and concentrations of the three substances in the air samples and the seasonal variability for some of them.

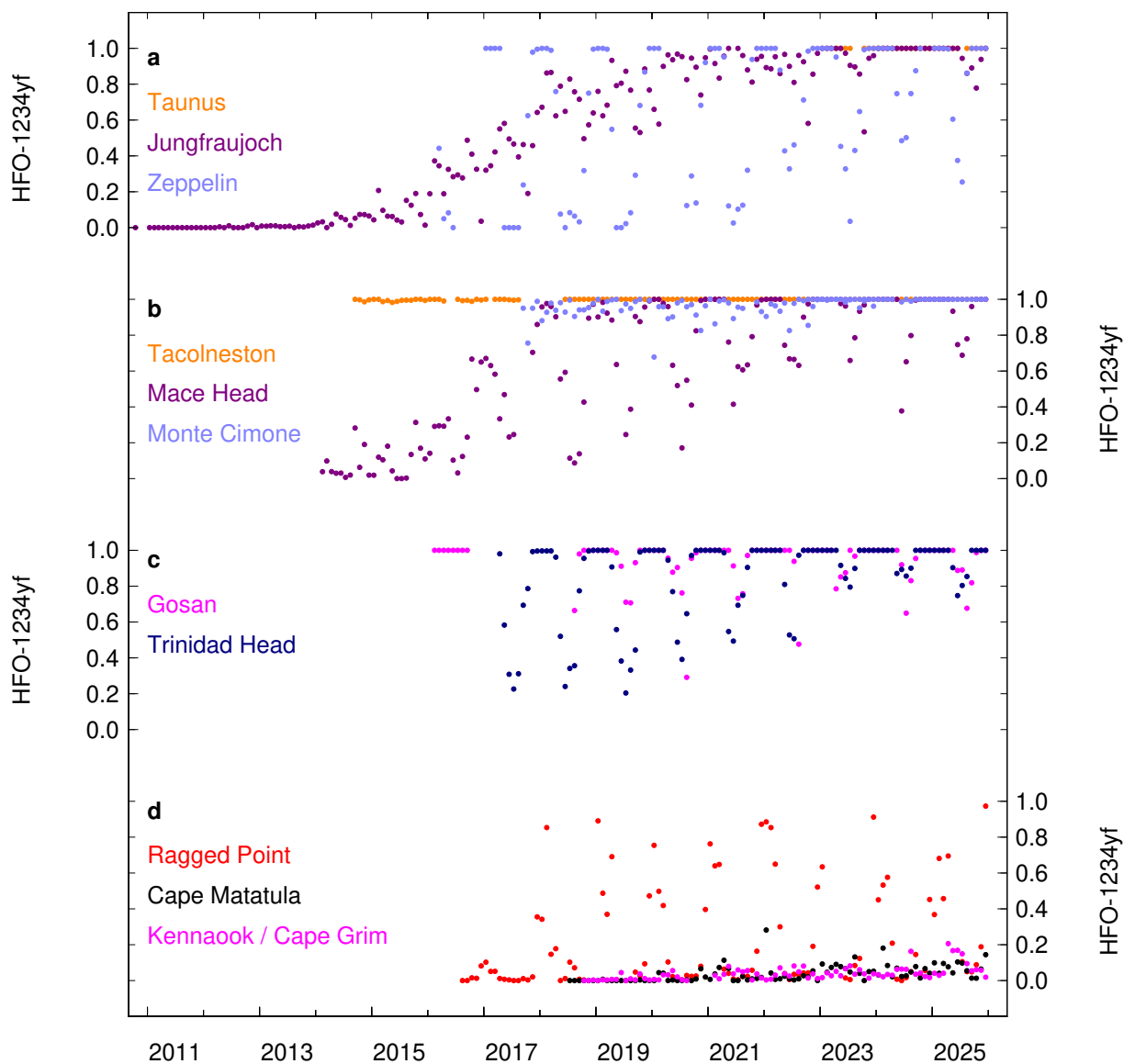


Figure S1. Ratio of the number of detectable to total measurements (monthly bins) for HFO-1234yf from AGAGE stations.

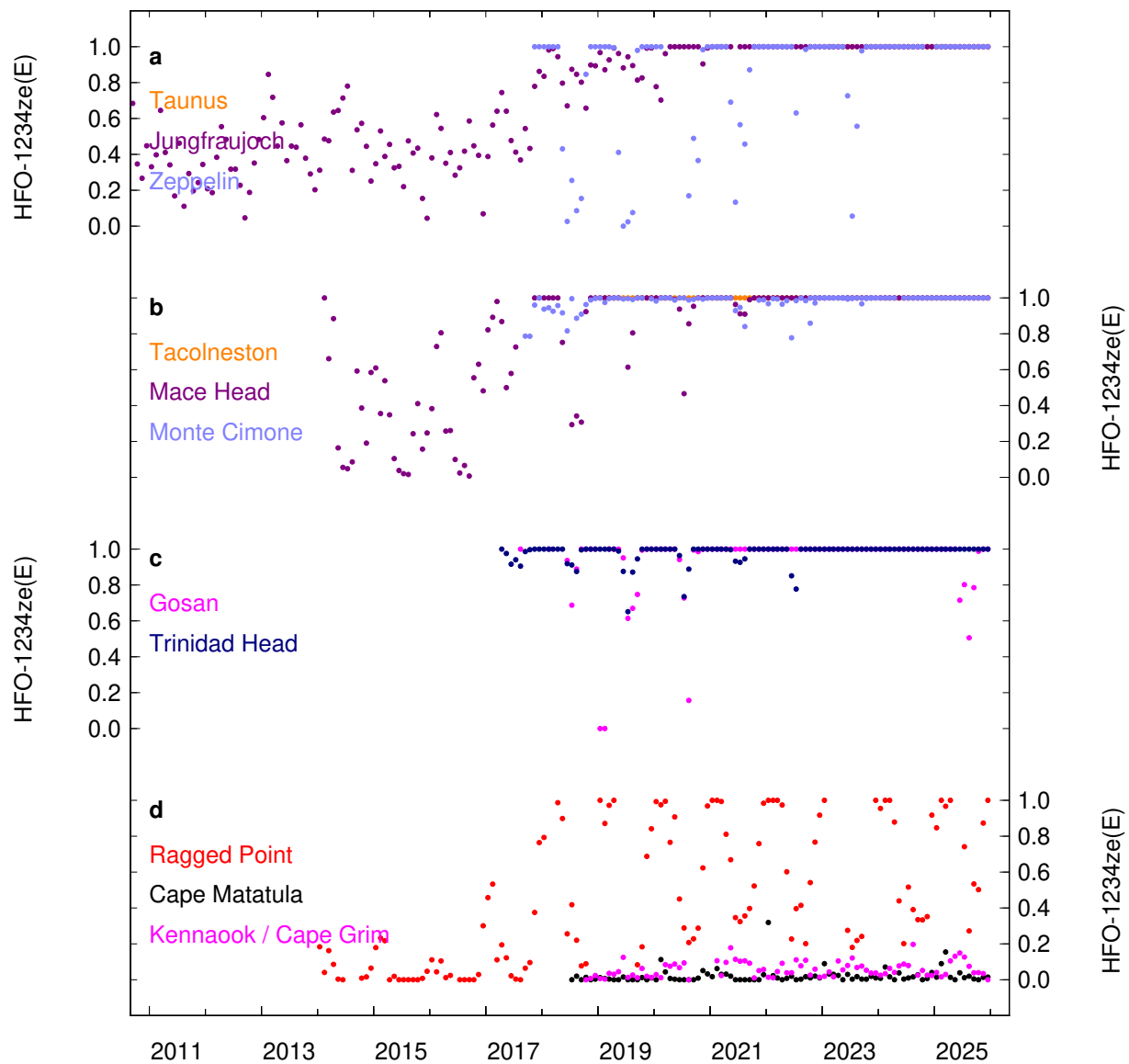


Figure S2. Ratio of the number of detectable to total measurements (monthly bins) for HFO-1234ze(E) from AGAGE stations.

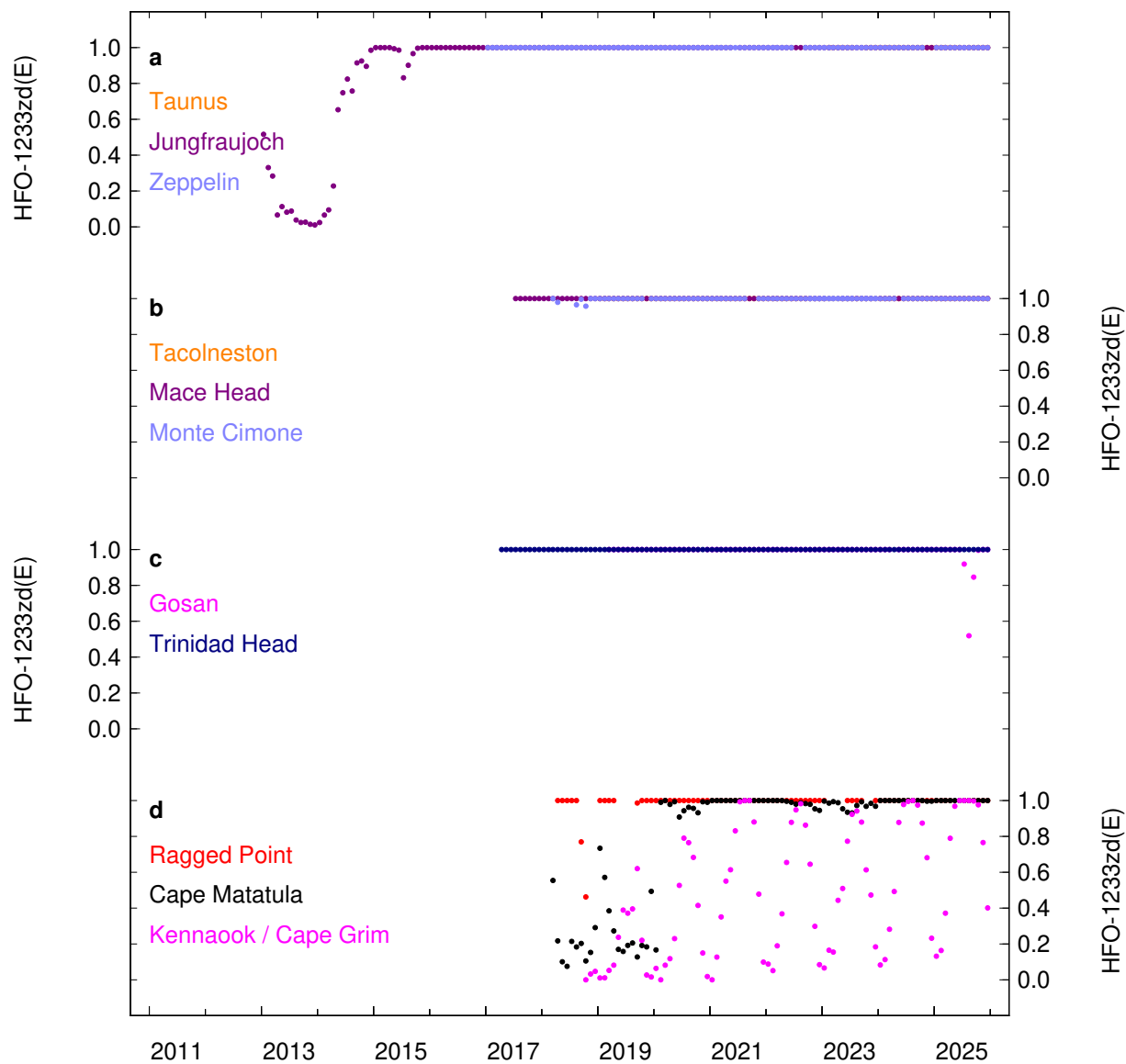


Figure S3. Ratio of the number of detectable to total measurements (monthly bins) for HCFO-1233zd(E) from AGAGE stations.

5 S2 Comparison of the pollution ratios at selected sites

Using the observations at Jungfraujoch, Mace Head, and Gosan, we inspect the pollution events of the haloolefins and compare these to the pollution events of HFC-134a. The purpose of this comparison is to illustrate the gradual replacement of HFC-134a by the haloolefins.

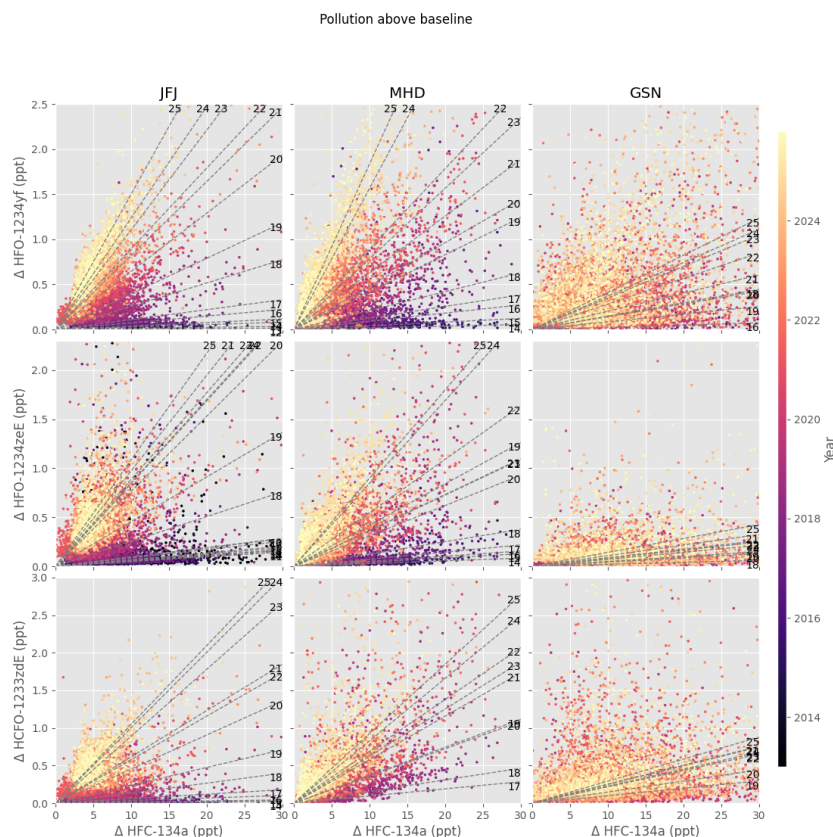


Figure S4. Pollution correlations against HFC-134a. Above-baseline (Δ) pollution mole fraction are determined for the haloolefins and HFC-134a using a baseline detection algorithm (Phyton `pspline_arpls` Erb, 2021; Baek et al., 2015). The slopes of yearly binned Δ haloolefins / Δ HFC-134a are determined by linear regression using least square fitting techniques (orthogonal distance regression, forced through 0/0). Numbers on the dashed lines for the linear regressions denote the years. These ratio slopes increase over time for all three haloolefins. See main text and Fig. 3 for further interpretations.

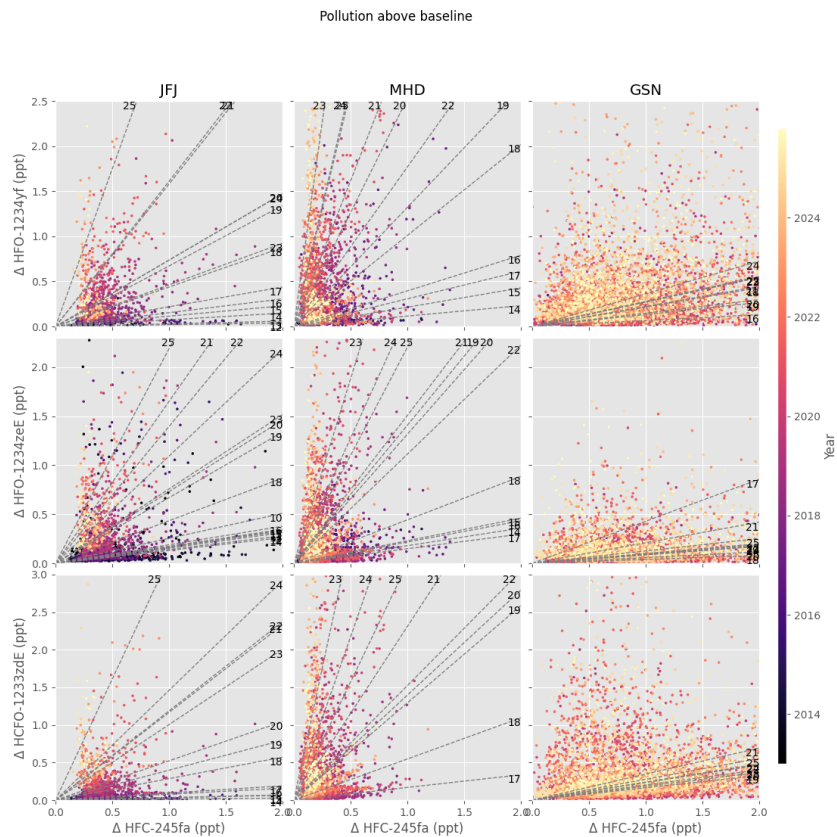


Figure S5. Pollution correlations against HFC-245fa. Above-baseline (Δ) pollution mole fraction are determined for the haloolefins and HFC-245fa using a baseline detection algorithm (Phyton pspline_arpls Erb, 2021; Baek et al., 2015). The slopes of yearly binned Δ haloolefins / Δ HFC-245fa are determined by linear regression using least square fitting techniques (orthogonal distance regression, forced through 0/0). Numbers on the dashed lines for the linear regressions denote the years. These ratio slopes increase over time for all three haloolefins. See main text and Fig. 3 for further interpretations.

S3 Observations at King Sejong, Antarctica

- 10 Observations of the three haloolefins are also available from the measurements of samples collected weekly at the South Korean Antarctic station King Sejong, King George Island (South Shetland Islands) and analyzed at Empa (Vollmer et al., 2011). Air samples have been collected since 2007, but until 2012 the measurement program was not set to measure haloolefins. During 2012–2016 the measurements showed obvious contamination of unclear origin for HFO-1234yf and HFO-1234ze(E) and were thus discarded. Every year, batch analyses are conducted for these samples, however, the acquisitions of the three haloolefins
- 15 are not activated for all samples to improve sensitivity and precision for chromatographically nearby eluting compounds. The results of the measurements are shown in Fig. S6 in comparison with in-situ results from Kennaook / Cape Grim and Cape Matatula (American Samoa). The yearly batch analyses are not following strict measurement protocol (in terms of analytical alternation with working standard measurements, analytical sample size) and mass spectrometric sensitivities are by nature not identical, such that peak detection levels may vary from year to year. Chromatographic peaks corresponding to mole fractions
- 20 <10 ppq (parts-per-quadrillion, femtomol mol⁻¹) for HFO-1234yf and HFO-1234ze(E) and <5 ppq for HCFO-1233zd(E) are not reliably related to the presence of the substance in the sample. Hence, most measurements are deemed non-detectable. Despite the absence of the haloolefins in most samples, these results are potentially useful for future modeling approaches as they provide a limitation to the presence of these substances in the sampled region. While for HFO-1234yf and HFO-1234ze(E) the record shows occasional detectable mole fraction, for HCFO-1233zd(E), which is the longest-lived of the three haloolefins,
- 25 a clear first appearance is detected, with an increasing number of detectable mole fractions over the last years, predominantly from samples collected during the austral winter. This is the first reported evidence that this compound has reached the Antarctic continent. The numeric results for the three compounds are provided as part of this study.

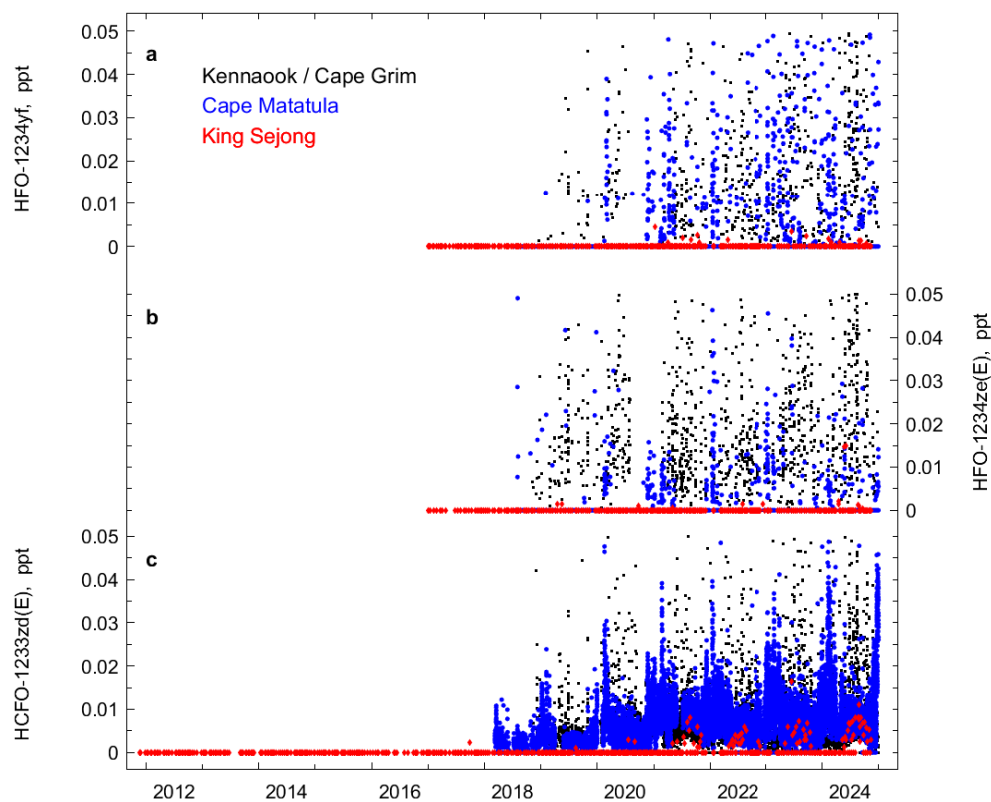


Figure S6. Observations of HFO-1234yf, HFO-1234ze(E) and HCFO-1233zd(E) from the South Korean Antarctic station King Sejong (red diamonds) compared to the in-situ records at Cape Matatula (blue circles) and Kennaoook / Cape Grim (black squares). Mole fractions >0.05 ppt are omitted from this figure. Results show mostly non-detectable haloolefins for King Sejong, but for HCFO-1233zd(E), some first detectable mole fractions are observed during the austral winter.

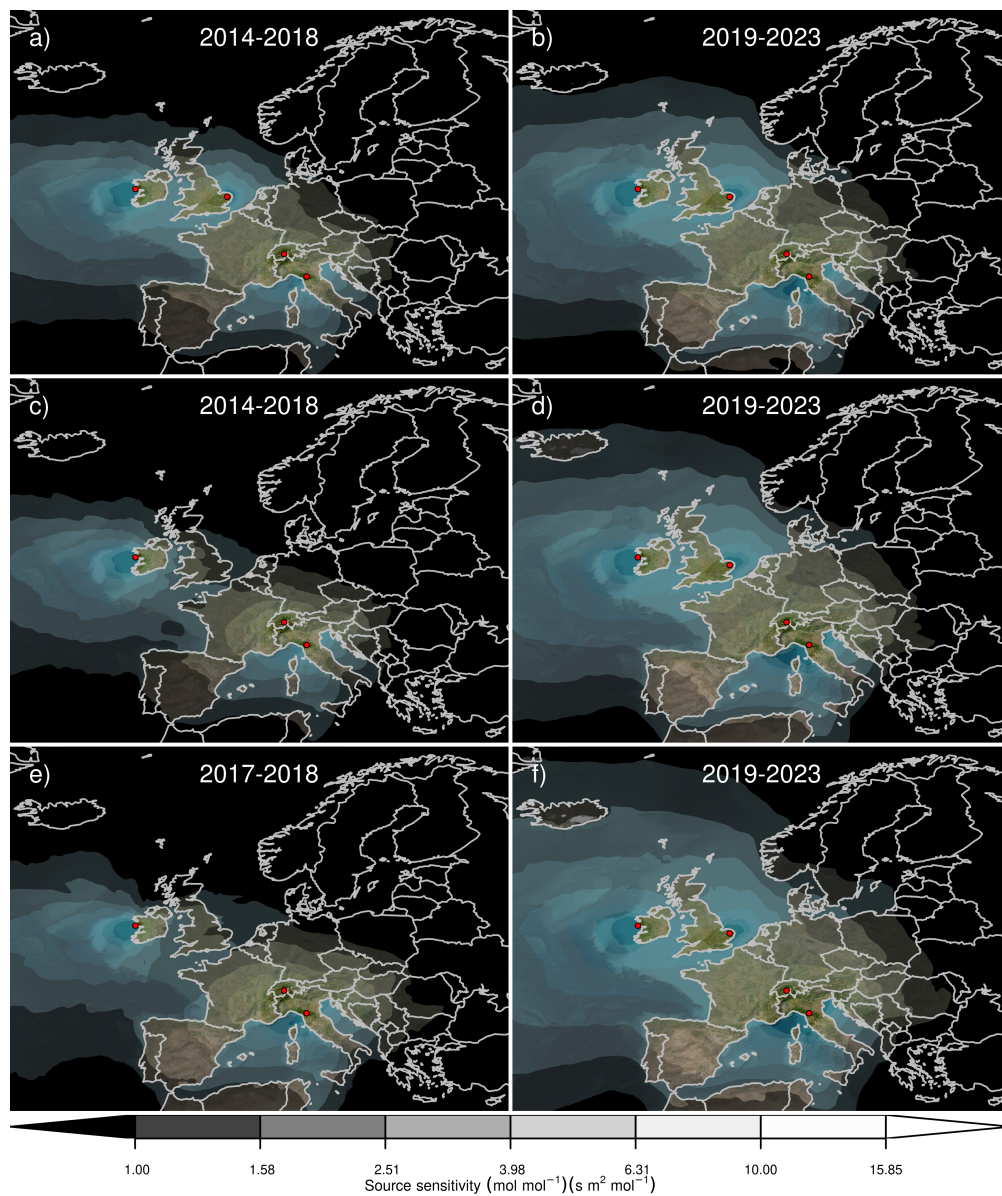


Figure S7. Average source sensitivity to HFO-1234yf (a,b), HFO-1234ze(E) (c,d), and HCFO-1233zd(E) (e,f) emissions as calculated by the NAME transport model for the years 2014-2018 (a,c,e) and 2019-2023 (b,d,f). For HCFO-1233zd(E) the earlier period only includes sensitivities from 2017 and 2018 since no observations were available before. Observing stations active in each period are marked as red dots. Areas with visible land surface represent regions for which emissions can be observed well from the network. Shaded or dark areas represent regions for which limited information on emissions can be obtained from the network.

S5 Effects of atmospheric lifetimes

- 30 The atmospheric lifetimes of HFO-1234yf, HFO-1234ze(E), and HCFO-1233zd(E) are considerably shorter than those of e.g., HFCs, hence an additional calculation is made to account for their degradation in the atmosphere over the model simulation. The rates of their atmospheric decay are based on calculations by Henne et al. (2012) using OH fields and FLEXPART simulations to derive HFO-1234yf monthly mean lifetimes. The resulting monthly mean lifetimes are given in Table S1 and are valid for a release in Europe. The effects of including lifetimes in the transport model on inverse emission estimates is shown
- 35 in Fig. S8. It can be seen that a non-negligible bias in posterior emissions occurs when this atmospheric degradation is not accounted for, with the expected largest discrepancy for the shorter-lived HFO-1234yf and HFO-1234ze(E), and with less effect for the longer-lived HCFO-1233zd(E).

Table S1. Atmospheric lifetimes (in days) for HFO-1234yf ($\text{CF}_3\text{CF}=\text{CH}_2$), HFO-1234zeE (*trans*- $\text{CF}_3\text{CH}=\text{CHF}$), and HCFO-1233zdE (*trans*- $\text{CF}_3\text{CH}=\text{CHCl}$).

Compound	Jan	Feb	Mar	Apr	May	Jun	Jul	Aug	Sep	Oct	Nov	Dec
HFO-1234yf	35.6	24.3	14.1	7.8	4.8	3.6	3.7	4.7	7.9	14.9	30.8	41.8
HFO-1234ze(E)	56.3	38.4	22.3	12.3	7.7	5.7	5.9	7.4	12.4	23.5	48.8	66.1
HCFO-1233zd(E)	125.6	85.7	49.8	27.5	17.1	12.8	13.2	16.5	27.8	52.5	108.9	147.6

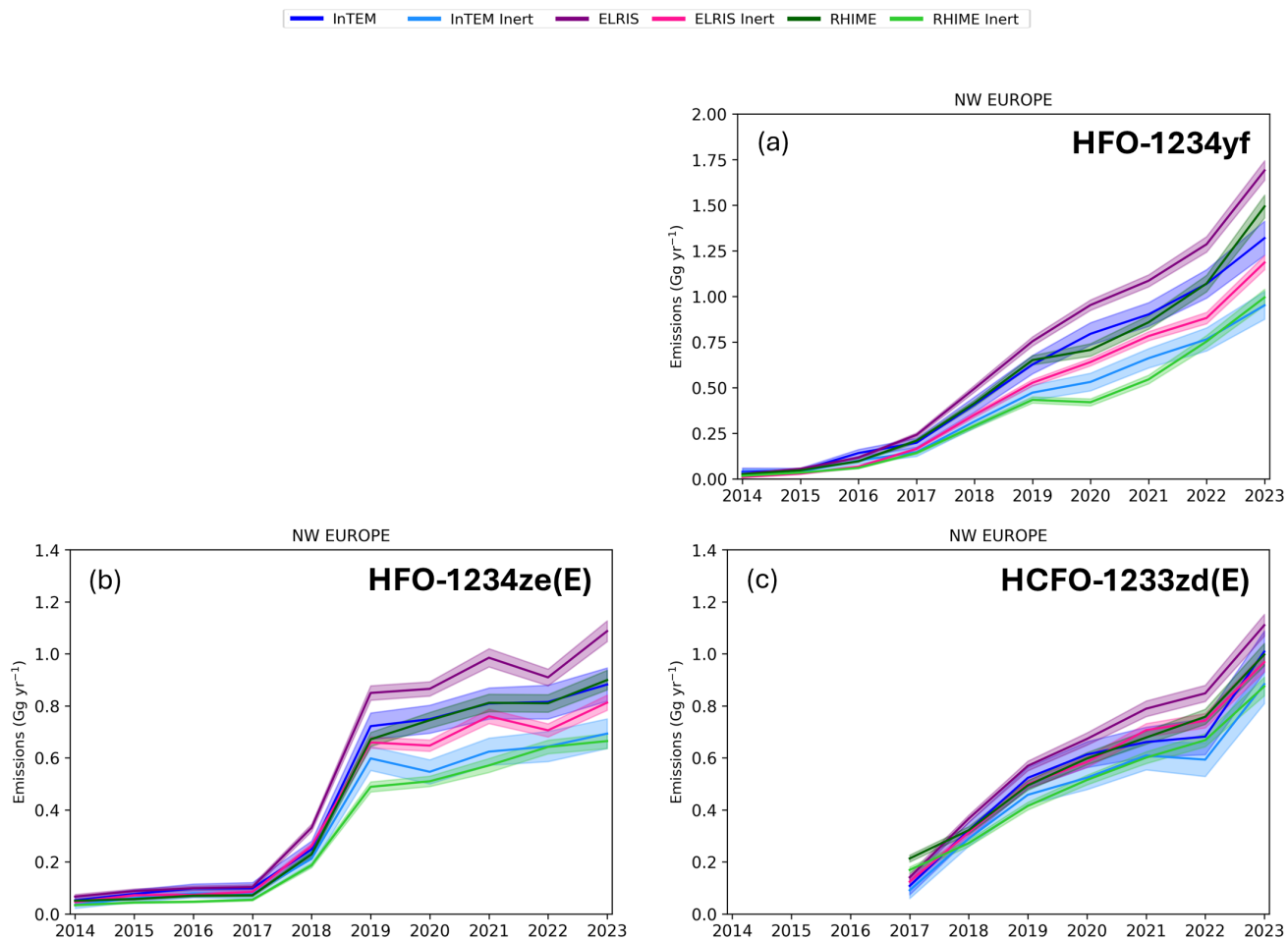


Figure S8. Comparison of emissions of (a) HFO-1234yf, (b) HFO-1234ze(E) and (c) HCFO-1233zd(E) from NW Europe for the lifetimes used in this work versus inertness. Significant differences for the two approaches demonstrate the need to include degradation/lifetime in the inverse methods approach.

S6 Prior flux sensitivity test

40 A sensitivity test was conducted to evaluate the impact of the spatial distribution of prior fluxes on the posterior emission estimates. Two prior flux maps were used: the first was the base case where emissions were distributed by population density, and the second was a flat prior where emissions were uniformly distributed over the land surface. In both cases the emissions were scaled to produce a total annual emission of 1 Gg for NW Europe. The posterior emission estimates using both prior maps are shown as timeseries in Fig. S9 and as spatial distributions in Fig. S10. It can be seen that the choice of prior has a minimal impact on the posterior emissions for all three models.

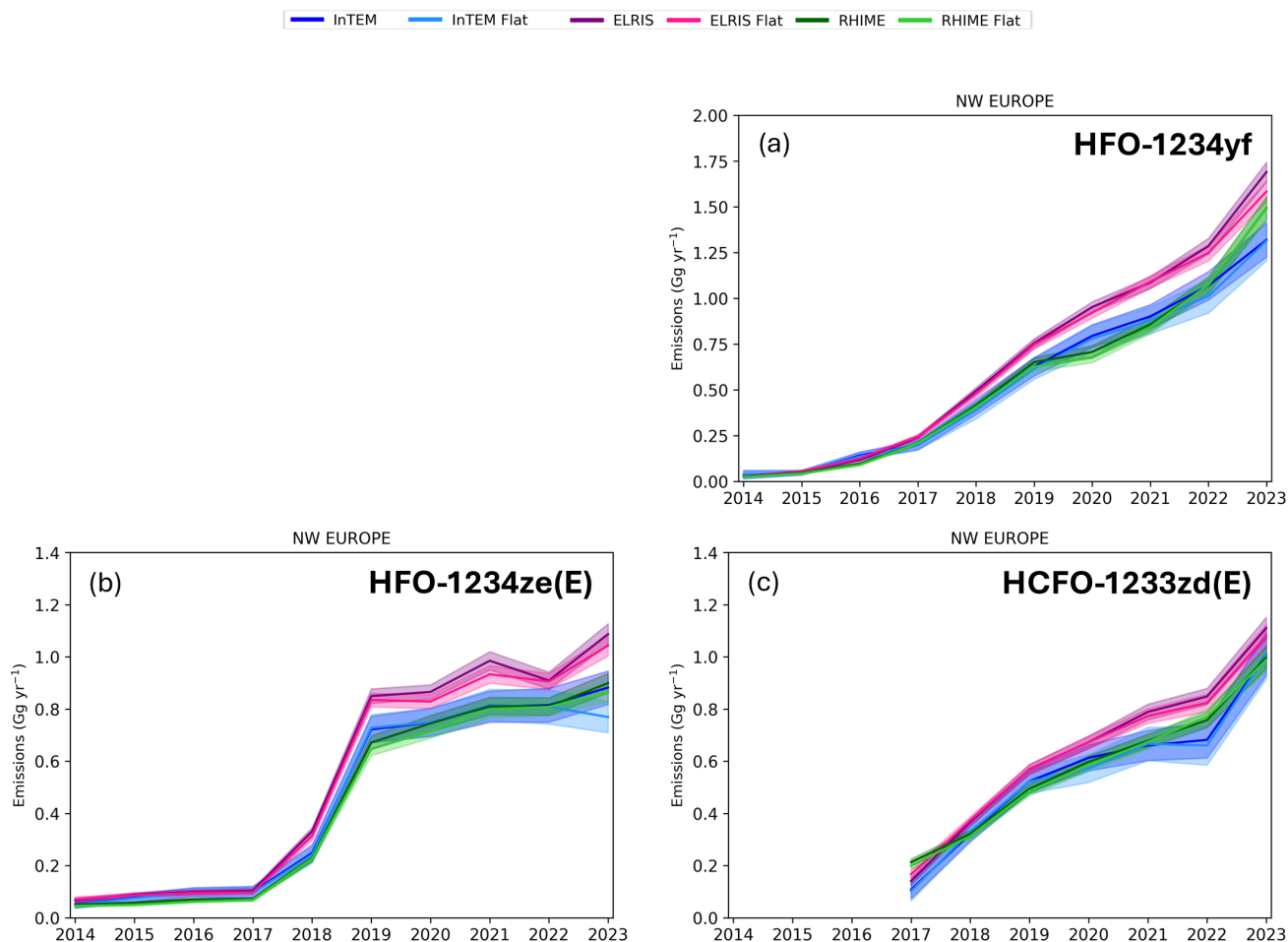
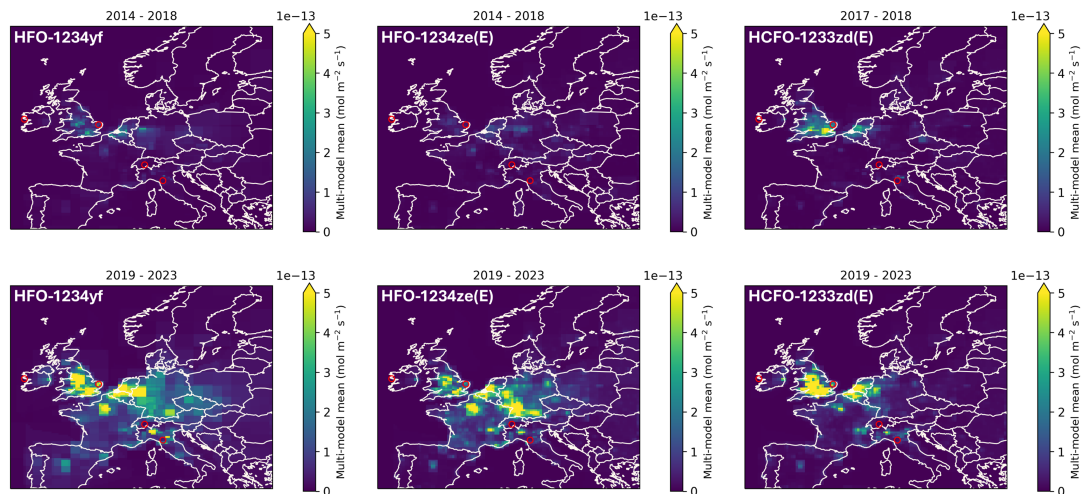


Figure S9. Impact of prior emission distribution for (a) HFO-1234yf, (b) HFO-1234ze(E) and (c) HCFO-1233zd(E) on posterior NW Europe emissions. Here the base case (using a population prior) is compared with the use of a flat land prior. Total posterior emissions for a given model do not have a significant dependence on the prior spatial distribution.

Results using population prior



Results using flat prior

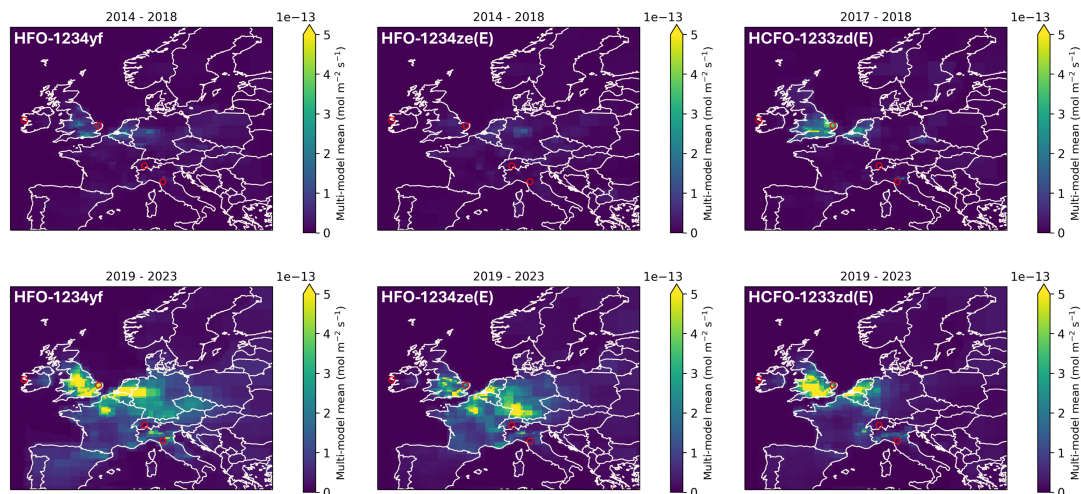


Figure S10. Spatial distribution maps for Northwest (NW) European comparing the population-based and the flat priors. Emissive fluxes of HFO-1234yf, HFO-1234ze(E) and HCFO-1233zd(E) for the periods 2014–2018 (2017–2018 for HCFO-1233zd(E)) in the respective upper panels and for 2019–2023 in the lower panels. Red circles denote measurement sites and are, from west to east, Mace Head (Ireland), Tacolneston (UK), Jungfrauoch (Switzerland), and Monte Cimone (Italy).

Emissions are shown for the individual countries/regions UK (Fig. S11), France (Fig. S12), Germany (Fig. S13), and the Benelux countries (Belgium, The Netherlands, and Luxembourg, Fig. S14).

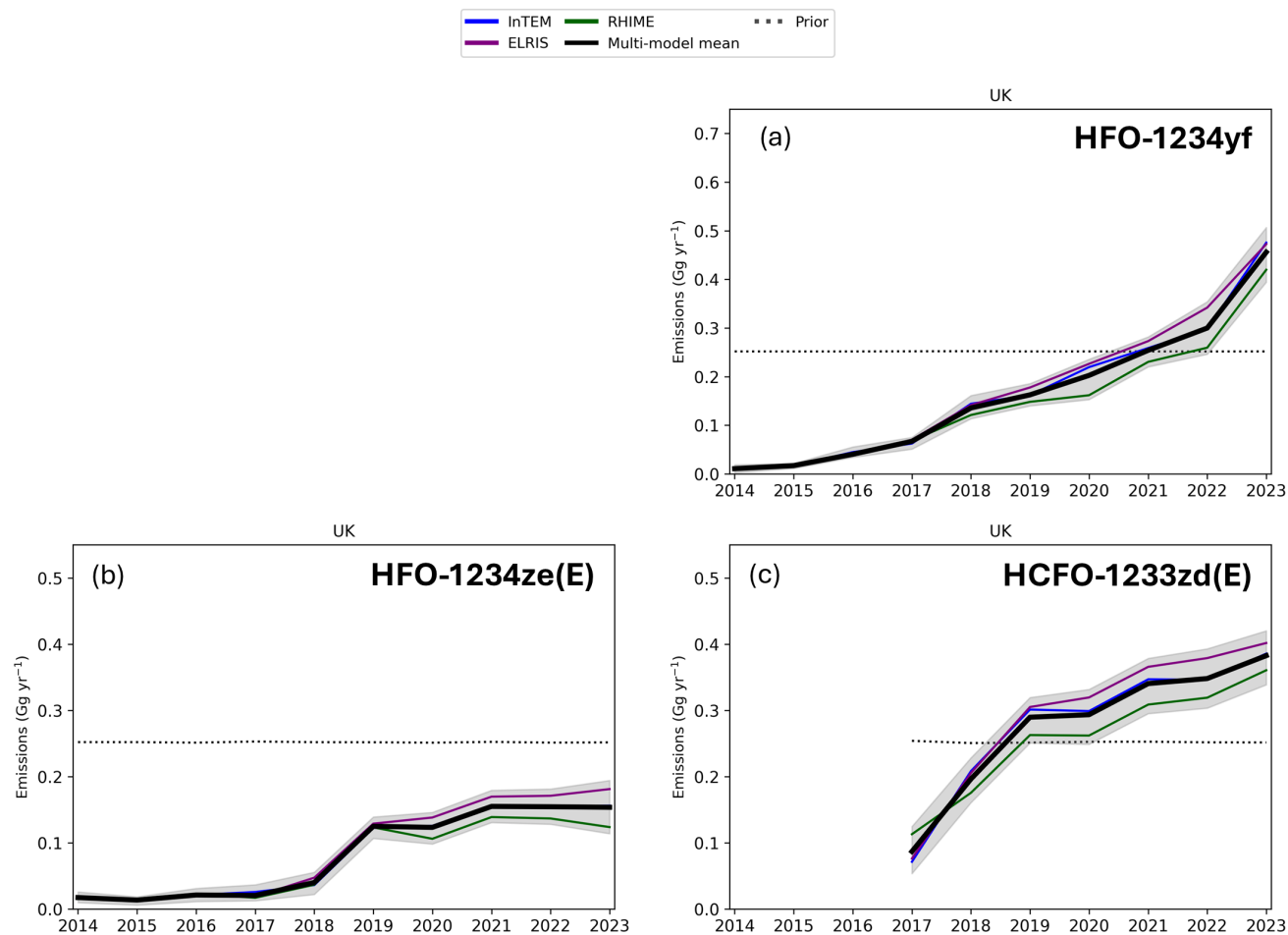


Figure S11. Emissions of HFO-1234yf, HFO-1234ze(E), and HCFO-1233zd(E) from the United Kingdom (UK), including England, Scotland, Wales and Northern Ireland. Emissions are shown for the three model approaches InTEM, ELRIS, and RHIME and for their mean, including an uncertainty for that mean (see Fig. 6 for details).

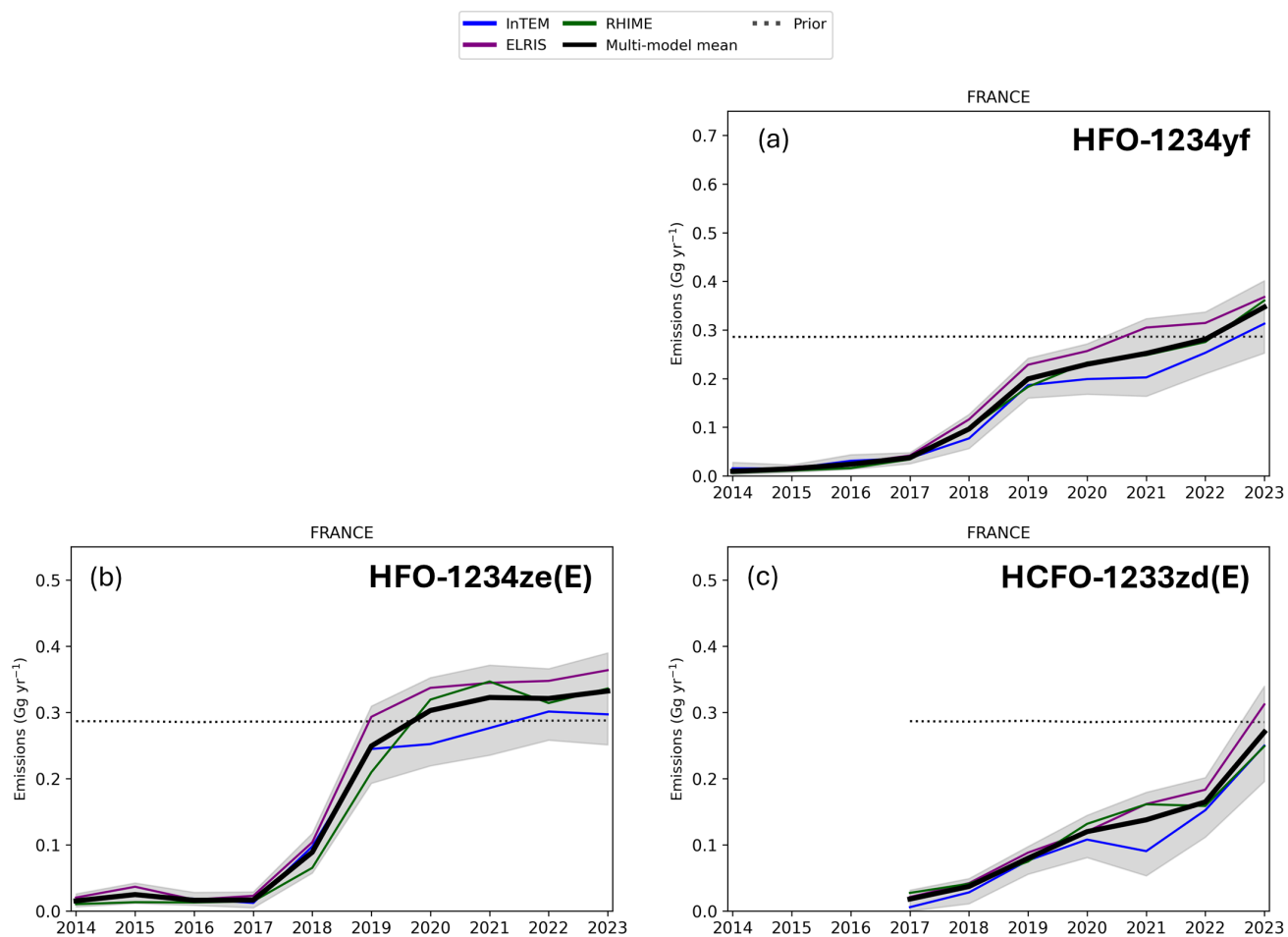


Figure S12. Emissions of HFO-1234yf, HFO-1234ze(E), and HCFO-1233zd(E) from France (see Fig. 6 for details).

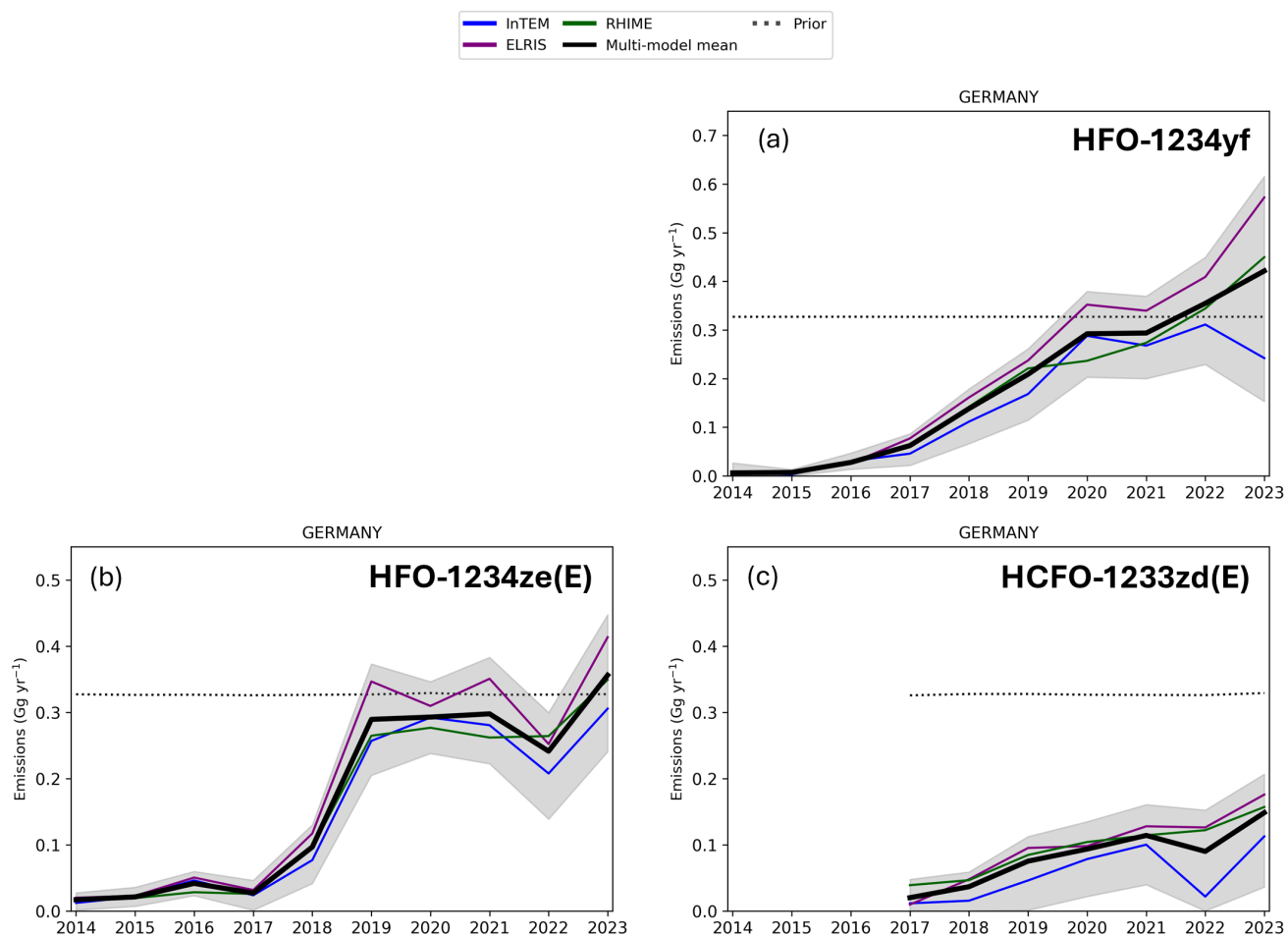


Figure S13. Emissions of HFO-1234yf, HFO-1234ze(E), and HCFO-1233zd(E) from Germany (see Fig. 6 for details).

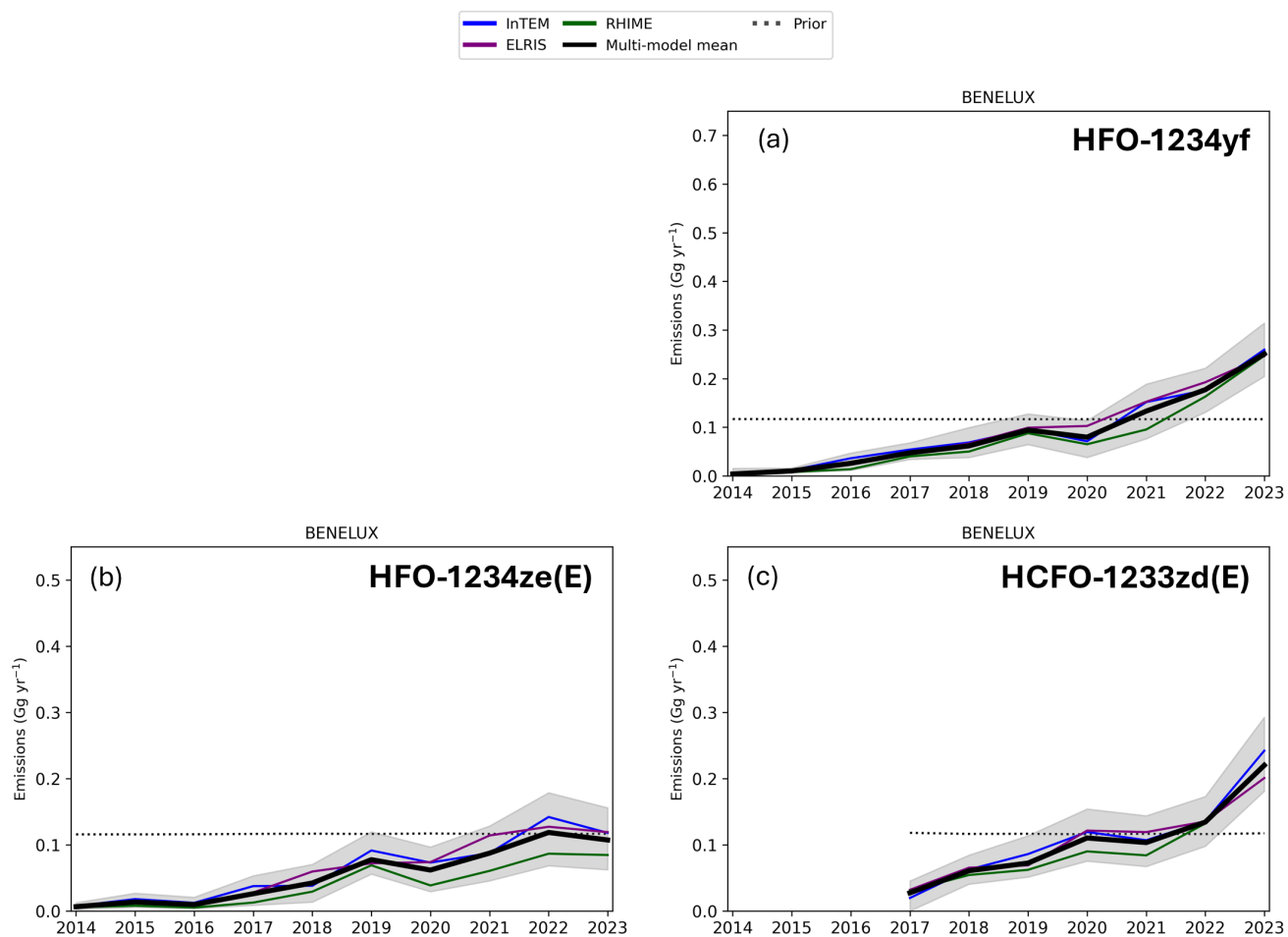


Figure S14. Emissions of HFO-1234yf, HFO-1234ze(E), and HCFO-1233zd(E) from the Benelux countries (see Fig. 6 for details).

S8 Instrument comparison for the Monte Cimone Station

At the Monte Cimone (CMN) station, the older ADS instrument (Maione et al., 2013) was run in overlap with the Medusa-GCMS for about 14 months (Oct 2022–Dec 2023) to track the transition between the two set-ups and investigate their differences. Both instruments used the same working standard (quaternary standard) and the same transfer calibration tertiary standard for the calibration of measurements; both systems sampled real air from the same main sampling line and flushing the terminal legs with their own pumping system; the timing of sample collection on the two instruments was not synchronized due to different chromatographic configurations and runtimes. The results of the comparison for the runs considered ‘matching runs’ (± 10 min) are summarized below (Figs S15–S17 and Tables S2 and S3). The vertical bars, which are shown in the plot, are the measurement precisions of the bracketing standards during analysis and not the precisions of the air measurements (which would be difficult to determine). The precisions for the air measurements are likely poorer than those indicated here because the standards are spiked with the HFOs (except that used in December 2023) thereby elevating the concentrations (to the range 1–1.5 ppt), leading to improved precisions, which can only be applied to the polluted air measurements in first approximation, as described in sect. 2.4.

Most of the observed differences fall within the combined measurement uncertainties, indicating that the two instruments are statistically consistent within their reported errors. Some deviations that exceed the expected uncertainty range are reported, particularly at higher concentrations, most likely due to some fast (short term) pollution transport events that the different instruments were not able to track because of the imperfect synchronization of the two sampling systems. Increasing the tolerance on time alignment from 10 min to 1 hr would result in a larger dataset but with poorer agreement, as expected due to the large variability on their atmospheric concentrations.

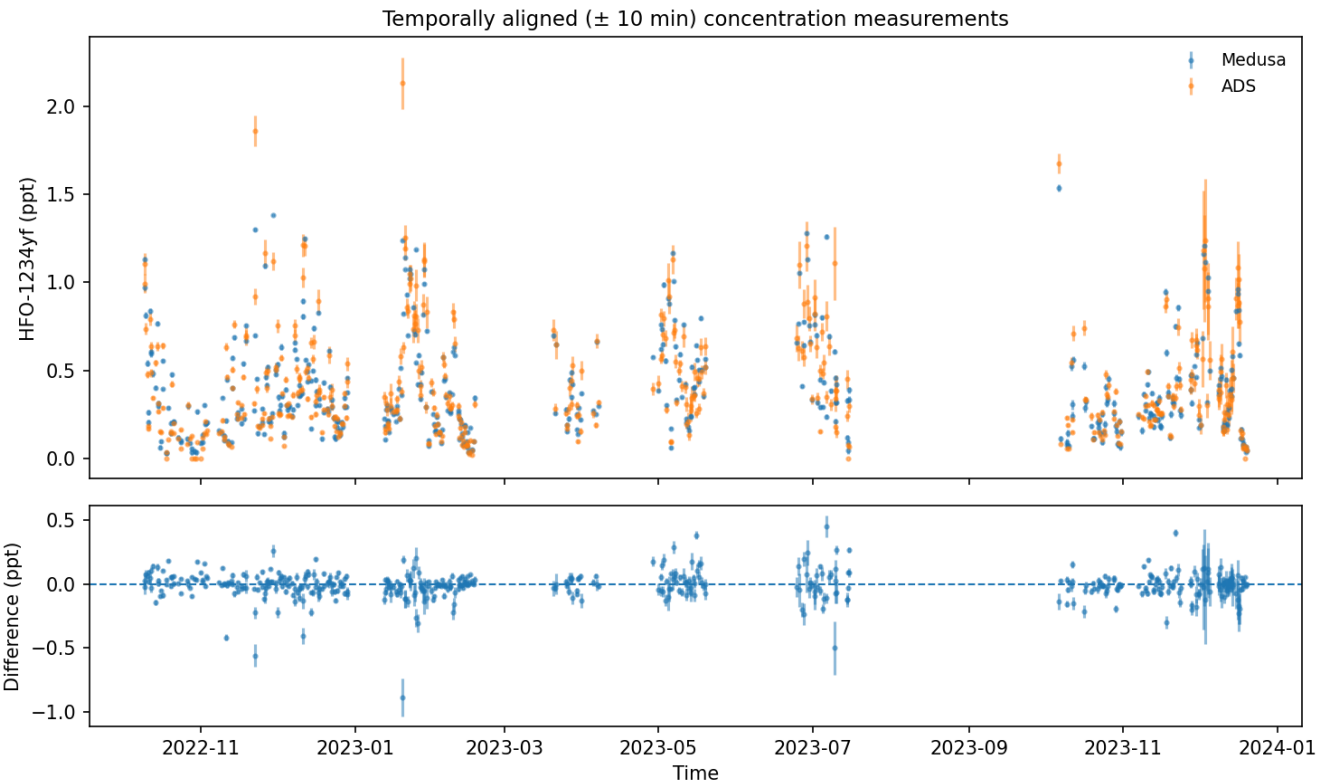


Figure S15. Records of HFO-1234yf from ADS and Medusa-GCMS instruments at Monte Cimone.

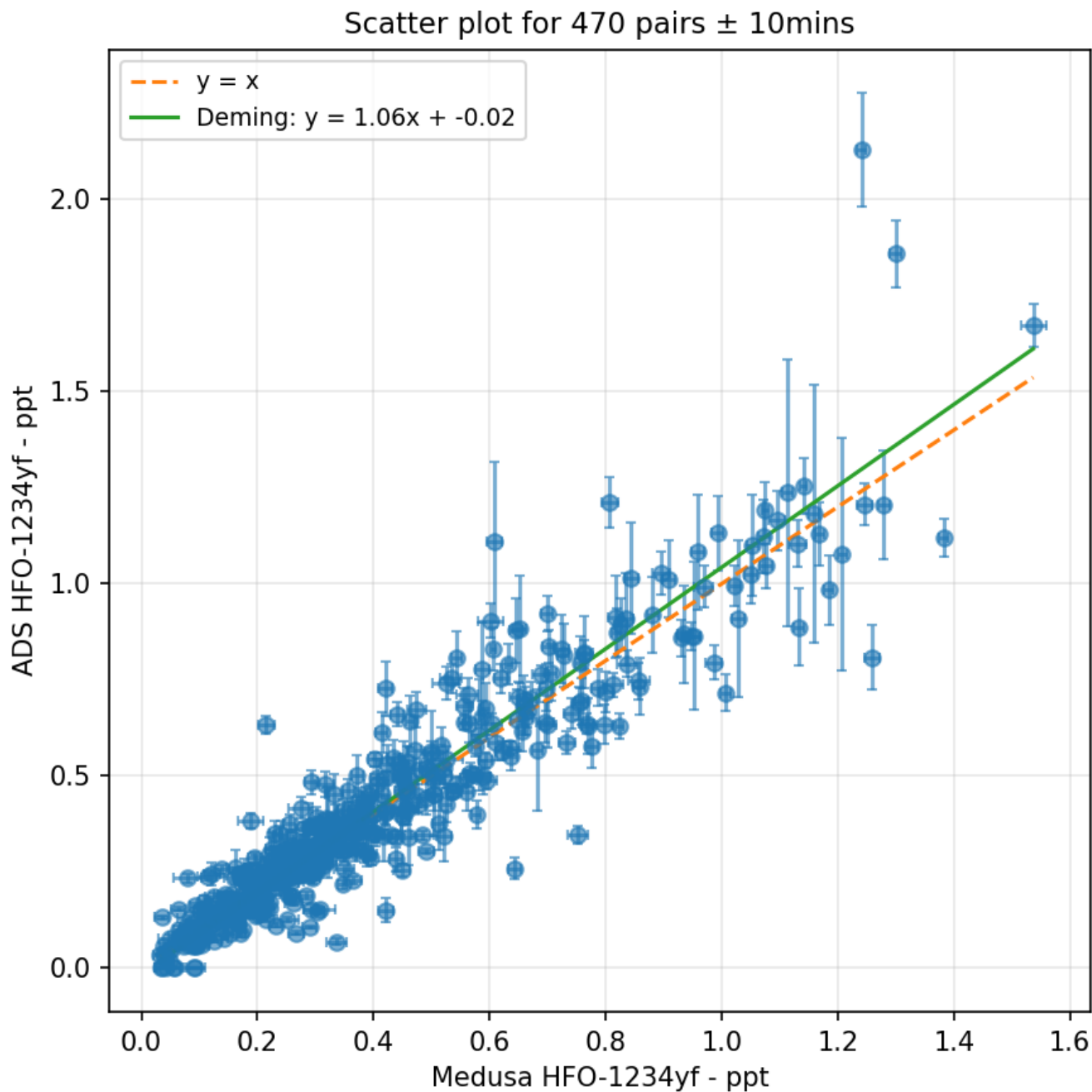


Figure S16. Scatterplot and linear regression for HFO-1234yf from ADS and Medusa-GCMS instruments at Monte Cimone.

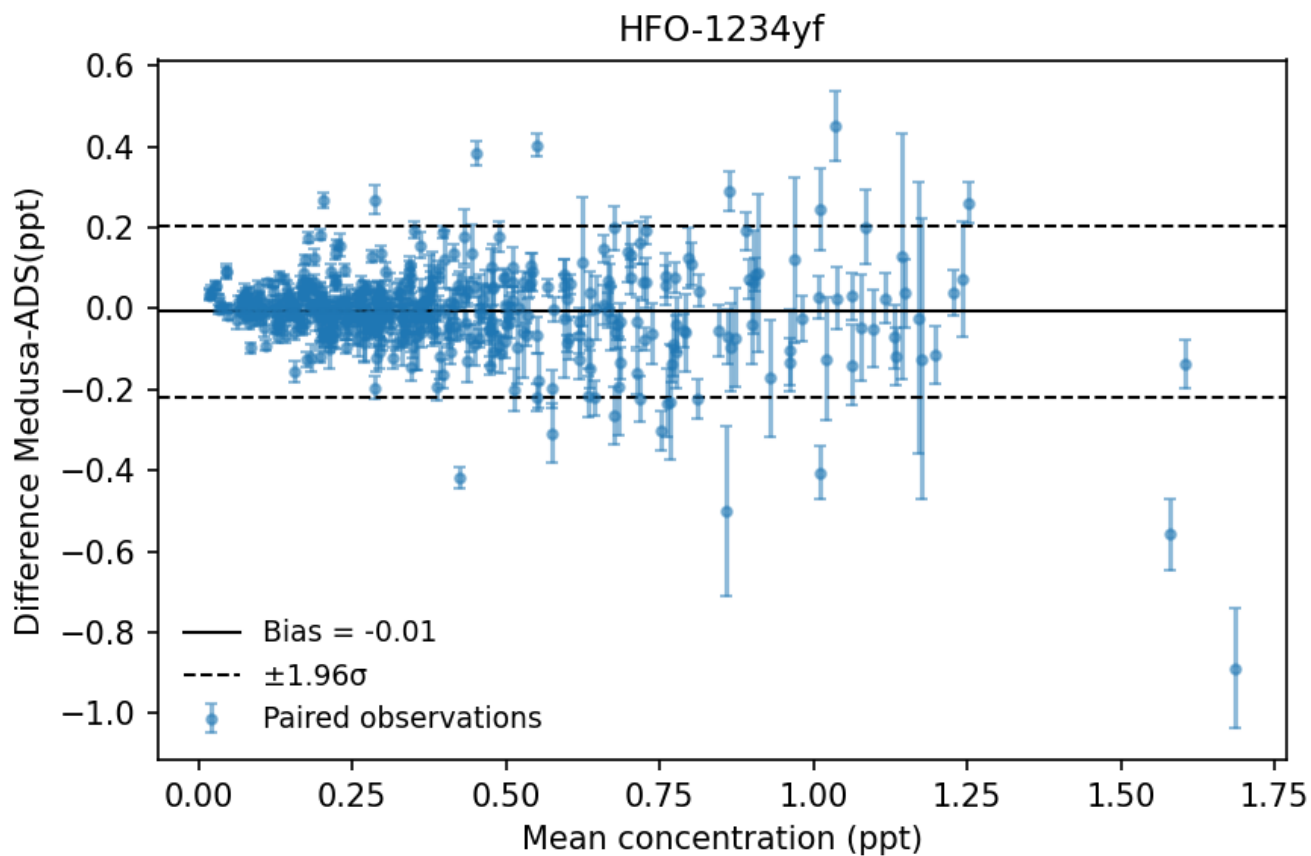


Figure S17. HFO-1234yf mole fraction difference vs mean mole fraction, between ADS and Medusa-GCMS instruments at Monte Cimone.

Table S2. Statistical Evaluation of the Monte Cimone ADS vs Medusa results for 10-min matching windows, for HFO-1234y, HFO-1234ze(E), and HCFO-1233zd(E).

Compound	HFO-1234yf	HFO-1234ze(E)	HCFO-1233zd(E)
N	470	478	474
Bias	-0.007	-0.017	-0.007
RMSE ^a	0.108	0.105	0.106
MAE ^b	0.068	0.063	0.053
Pearson r, p ^c	0.934, p<0.001	0.929, p<0.001	0.895, p<0.001
Spearman rho	0.937	0.921	0.944

a) RMSE: Root mean square error
b) MAE: mean absolute error
c) p-value test for uncorrelated systems

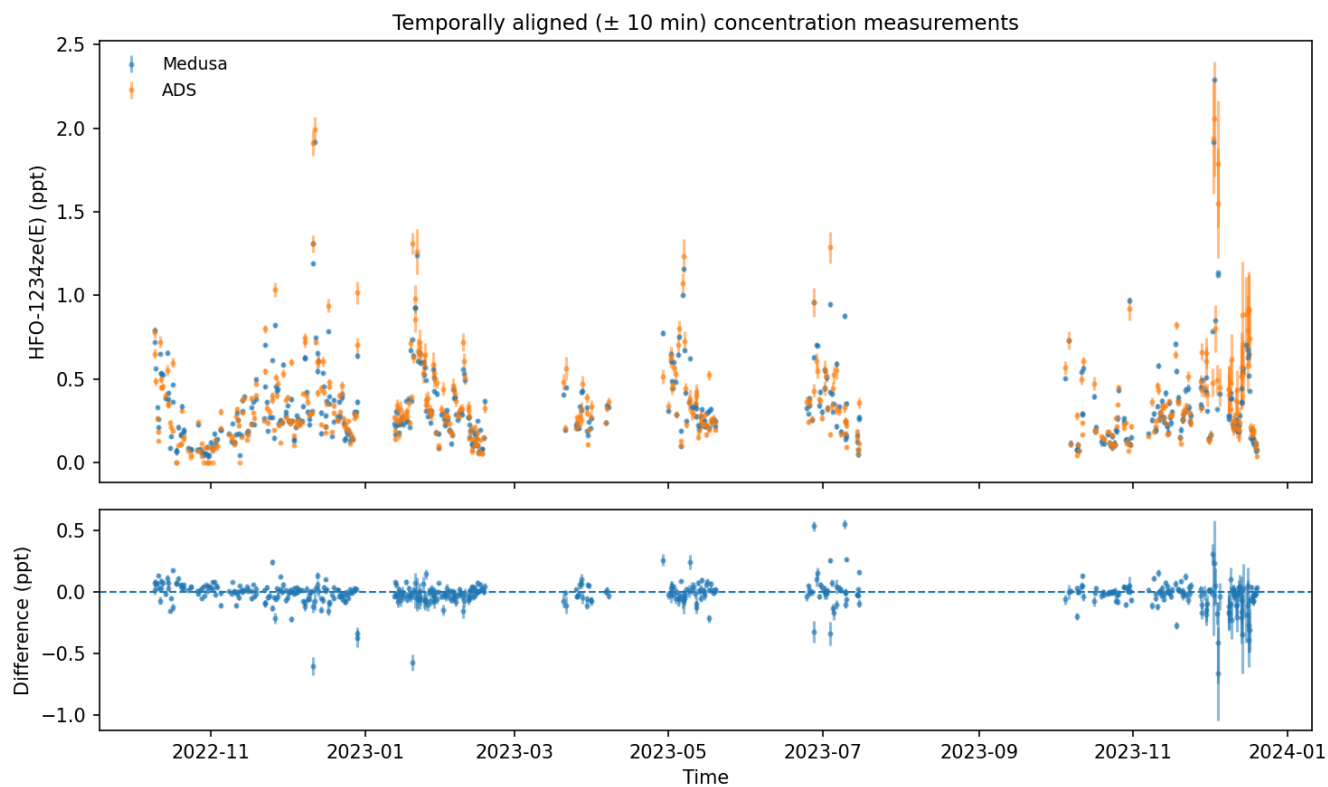


Figure S18. Records of HFO-1234ze(E) from ADS and Medusa-GCMS instruments at Monte Cimone.

Table S3. Statistical Evaluation of the Monte Cimone ADS vs Medusa results for 1-hr matching windows, for HFO-1234y, HFO-1234ze(E), and HCFO-1233zd(E).

Compound	HFO-1234yf	HFO-1234ze(E)	HCFO-1233zd(E)
N	2021	2054	2048
Bias	-0.008	-0.022	-0.014
RMSE ^a	0.151	0.216	0.154
MAE ^b	0.080	0.074	0.063
Pearson r, p ^c	0.908, p<0.001	0.812, p<0.001	0.880, p<0.001
Spearman rho	0.932	0.920	0.937

a) RMSE: Root mean square error
b) MAE: mean absolute error
c) p-value test for uncorrelated systems

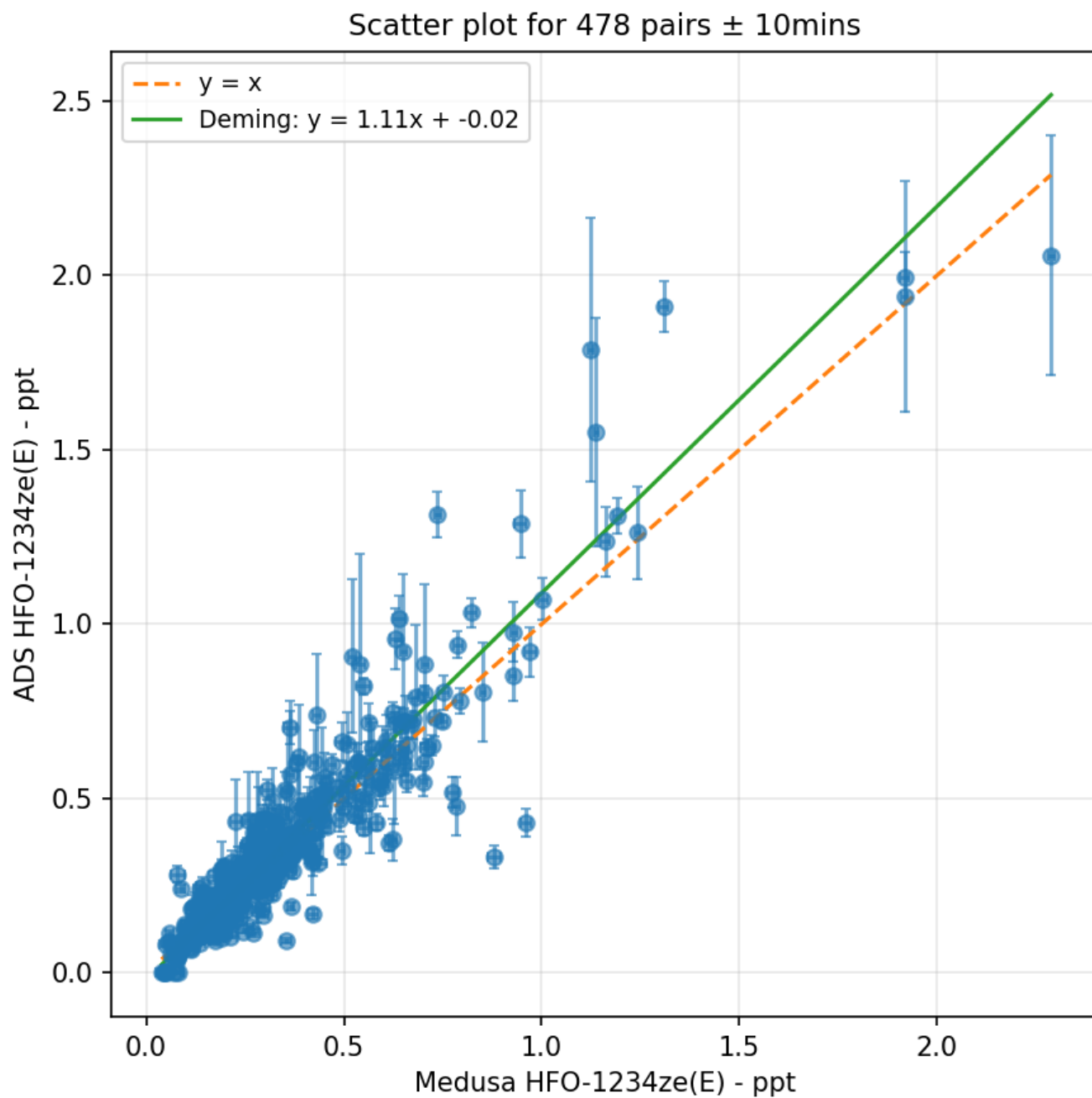


Figure S19. Scatterplot and linear regression for HFO-1234ze(E) from ADS and Medusa-GCMS instruments at Monte Cimone.

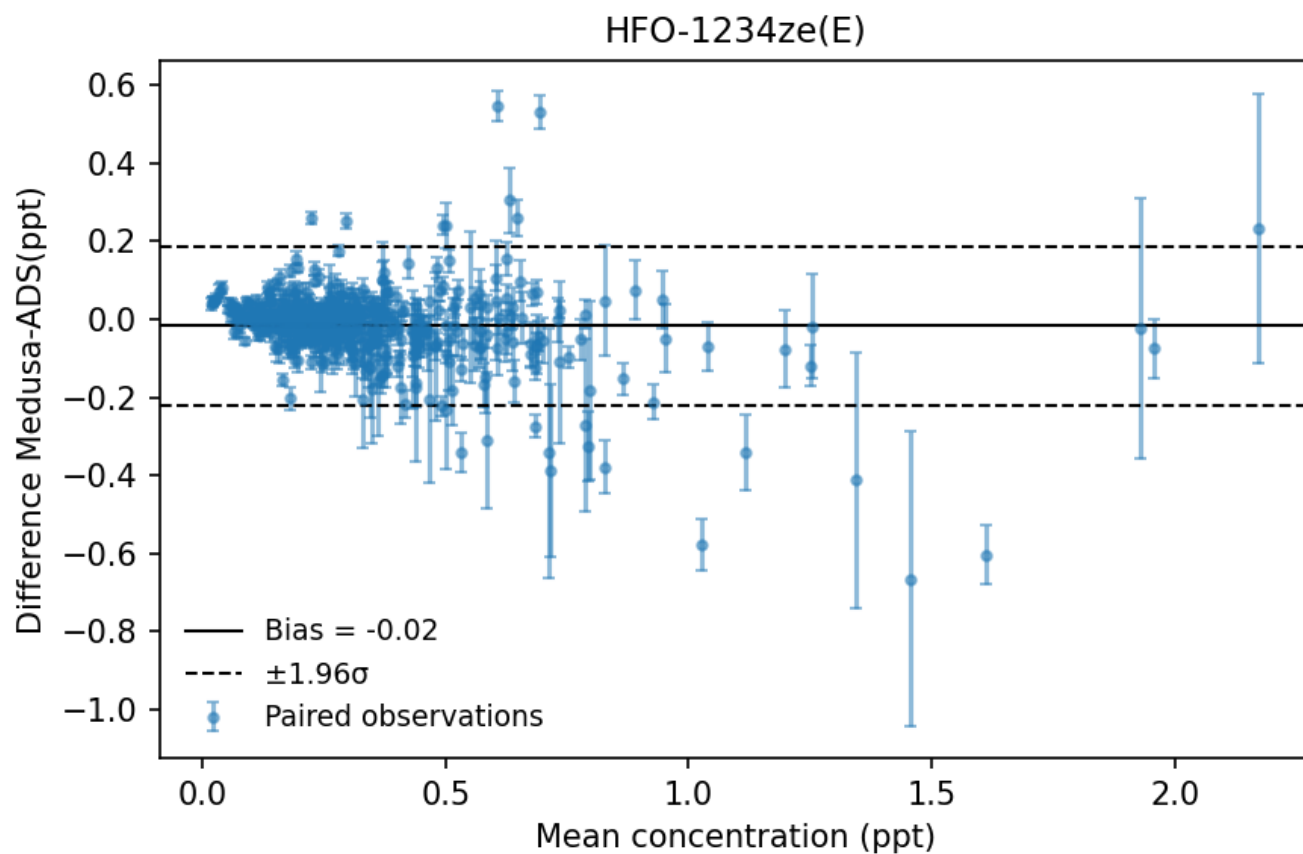


Figure S20. HFO-1234ze(E) mole fraction difference vs mean mole fraction, between ADS and Medusa-GCMS instruments at Monte Cimone.

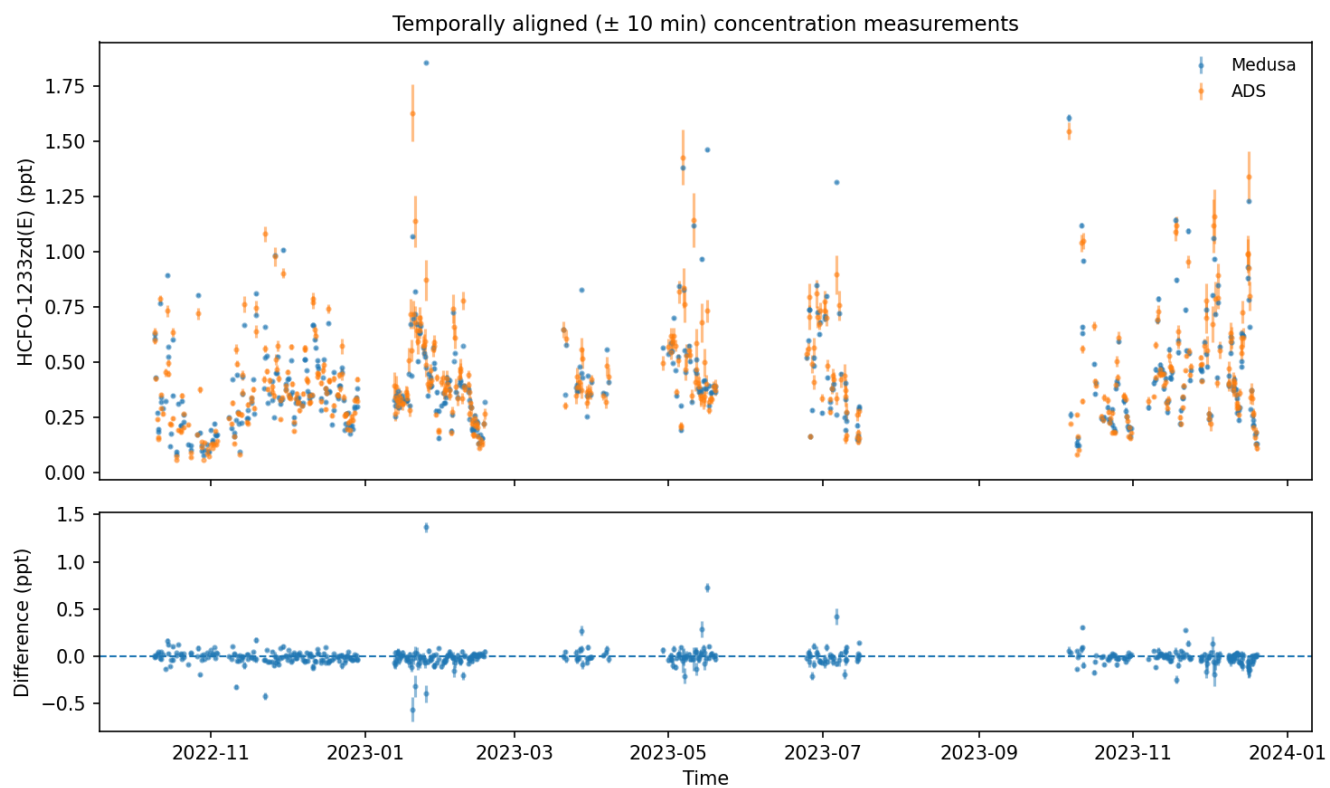


Figure S21. Records of HCFO-1233zd(E) from ADS and Medusa-GCMS instruments at Monte Cimone.

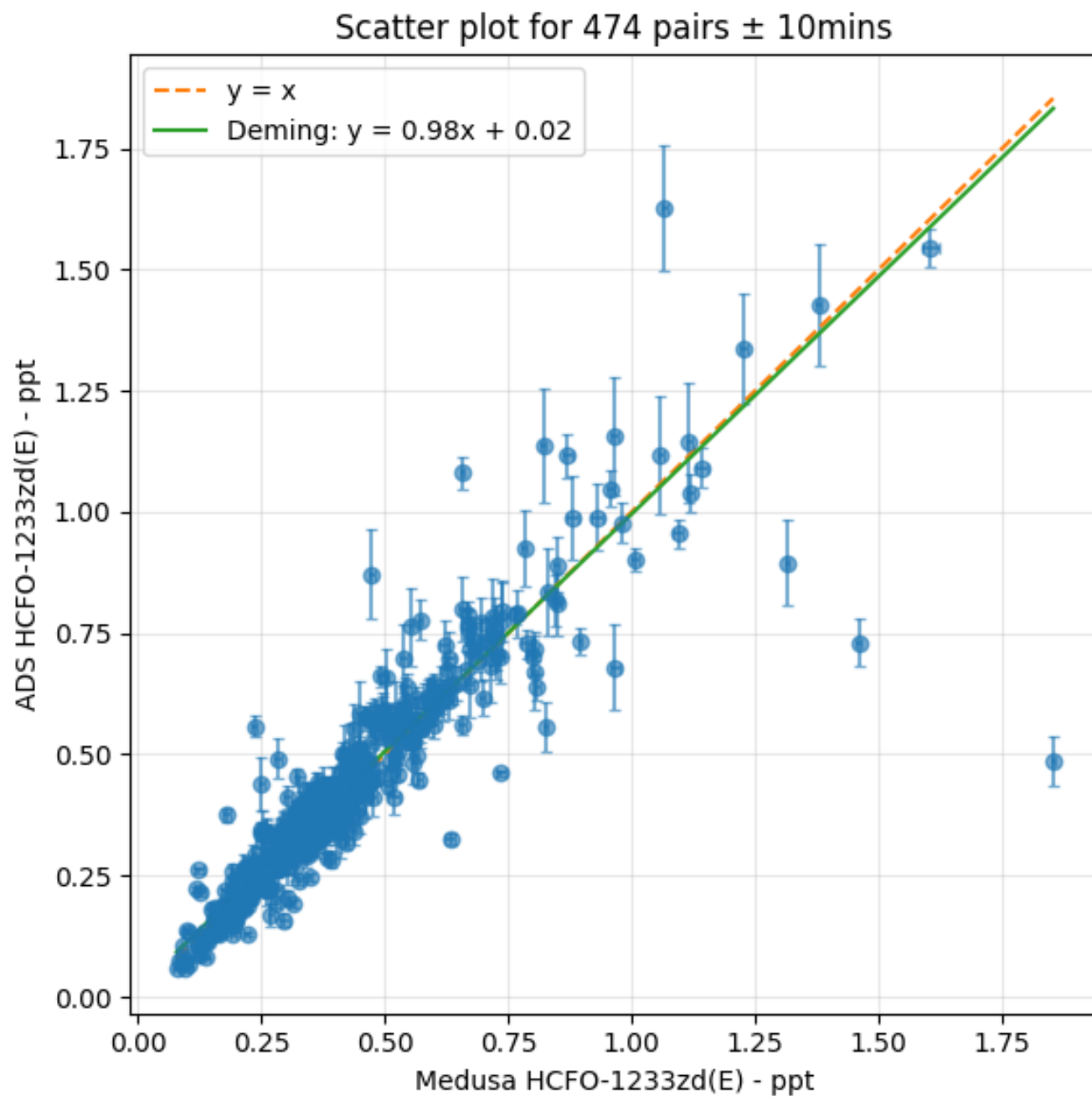


Figure S22. Scatterplot and linear regression for HCFO-1233zd(E) from ADS and Medusa-GCMS instruments at Monte Cimone.

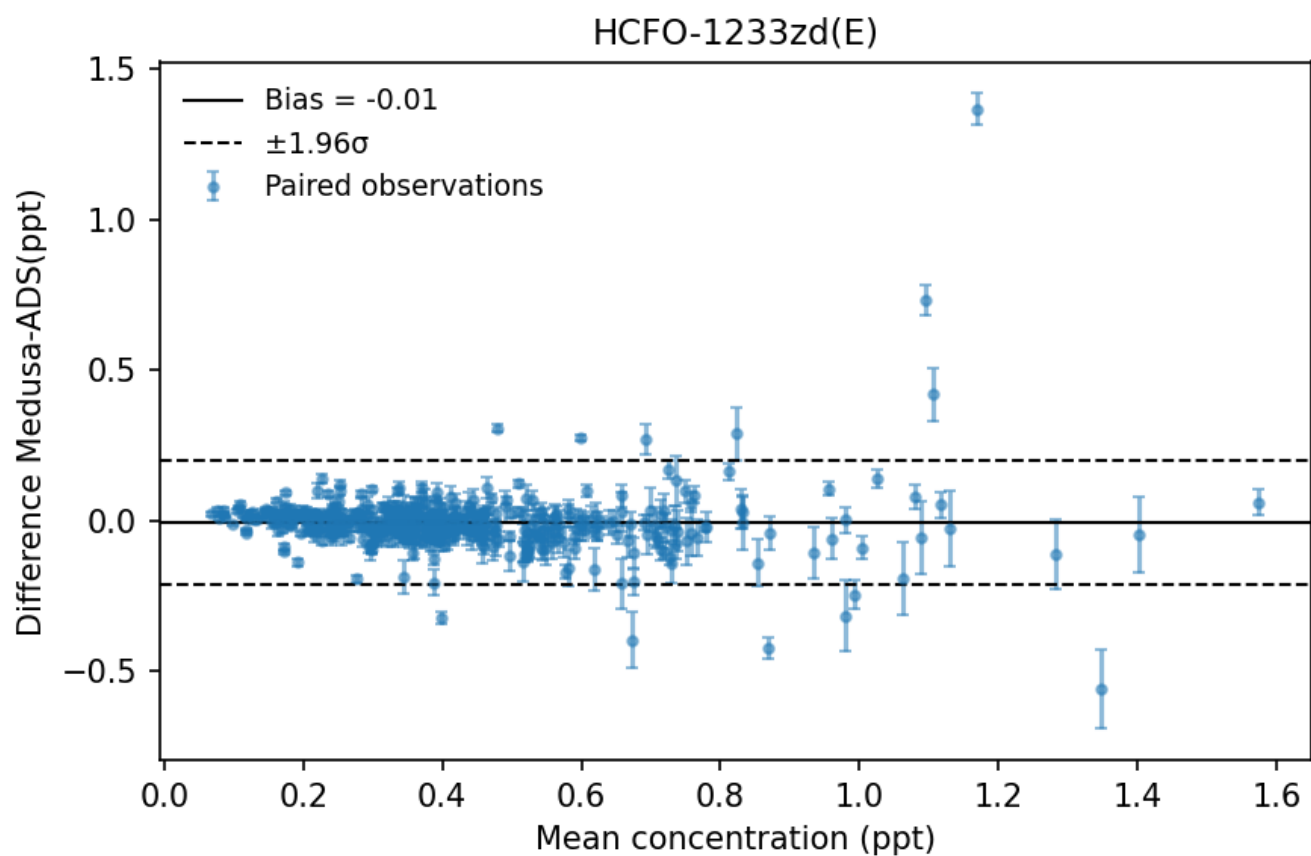


Figure S23. HCFO-1233zd(E) mole fraction difference vs mean mole fraction, between ADS and Medusa-GCMS instruments at Monte Cimone.

References

- Baek, S.-J., Park, A., Ahn, Y.-J., and Choo, J.: Baseline correction using asymmetrically reweighted penalized least squares smoothing, *Analyst*, 140, 250–257, <https://doi.org/10.1039/C4AN01061B>, 2015.
- 70 Erb, D.: pybaselines: A Python library of algorithms for the baseline correction of experimental data, <https://doi.org/10.5281/zenodo.5608581>, 2021.
- Henne, S., Shallcross, D. E., Reimann, S., Xiao, P., Brunner, D., O’Doherty, S., and Buchmann, B.: Future emissions and atmospheric fate of HFC-1234yf from mobile air conditioners in Europe, *Environ. Sci. Technol.*, 46, 1650–1658, <https://doi.org/10.1021/es2034608>, 2012.
- Maione, M., Giostra, U., Arduini, J., Furlani, F., Graziosi, F., Lo Vullo, E., and Bonasoni, P.: Ten years of continuous observations of
75 stratospheric ozone depleting gases at Monte Cimone (Italy) — Comments on the effectiveness of the Montreal Protocol from a regional perspective, *Sci. Tot. Environ.*, pp. 155–164, <https://doi.org/10.1016/j.scitotenv.2012.12.056>, 2013.
- Vollmer, M. K., Miller, B. R., Rigby, M., Reimann, S., Mühle, J., Krummel, P. B., O’Doherty, S., J., K., Rhee, T. S., Weiss, R. F., Fraser, P. J., Simmonds, P. G., Salameh, P. K., Harth, C. M., Wang, R. H. J., Steele, L. P., Young, D., Lunder, C. R., Hermansen, O., Ivy, D.,
80 Arnold, T., Schmidbauer, N., Kim, K.-R., Grealley, B. R., Hill, M., Leist, M., Wenger, A., and Prinn, R. G.: Atmospheric histories and global emissions of the anthropogenic hydrofluorocarbons HFC-365mfc, HFC-245fa, HFC-227ea, and HFC-236fa, *J. Geophys. Res.*, 116, D08304, <https://doi.org/10.1029/2010JD015309>, 2011.